Estimation of Skin Friction on the NASA BeVERLI Hill using Oil Film Interferometry

Conference Paper · January 2023

DOI: 10.2514/6.2023-0988

11 authors, including:

Vignesh Sundarraj
Virginia Tech (Virginia Polytechnic Institute and State University)
6 PUBLICATIONS **15** CITATIONS
SEE PROFILE

Aldo Gargiulo
Virginia Tech (Virginia Polytechnic Institute and State University)
20 PUBLICATIONS **77** CITATIONS
SEE PROFILE

Julie Duetsch-Patel
Virginia Tech (Virginia Polytechnic Institute and State University)
16 PUBLICATIONS **66** CITATIONS
SEE PROFILE

K. Todd Lowe
Virginia Tech (Virginia Polytechnic Institute and State University)
207 PUBLICATIONS **942** CITATIONS
SEE PROFILE

AIAA SciTech Forum
23-27 January 2023, National Harbor, MD & Online
AIAA SCITECH 2023 Forum

10.2514/6.2023-0988

Estimation of Skin Friction on the NASA BeVERLI Hill using Oil Film Interferometry

Vignesh Sundarraj*
Virginia Tech, Blacksburg, VA 24061,USA

Daniel MacGregor†
University of Toronto, Toronto, ON, M3H 5T6 Canada,

Aldo Gargiulo‡, Julie E. Duetsch-Patel§, Thomas Ozoroski¶,Tom Hallock‖,Aurelien Borgoltz**,Christopher J.Roy††, K. Todd Lowe‡‡, Máté Szőke §§ and William J. Devenport¶¶
Virginia Tech, Blacksburg, VA 24061,USA

Philippe Lavoie***
University of Toronto, Toronto, ON, M3H 5T6 Canada

Viscous drag reduction plays a vital role in increasing the performance of vehicles. However, there are only so many measurement techniques that can quickly and accurately measure this when compared to pressure drag measurement techniques. The current study makes use of one of the direct and robust measurement techniques that exist, called the Oil Film Interferometry (OFI) to estimate skin friction on the NASA/Virginia Tech BeVERLI (Benchmark Validation Experiment for RANS and LES Investigations) hill. This project aims to develop a detailed database of non-equilibrium, separated turbulent boundary layer flows obtained through wind tunnel experiments for CFD validation. Skin friction measurements are obtained at specific critical locations on the hill and in its close proximity. The challenges involved in obtaining skin friction data from these locations are discussed in detail. Detailed discussions on the experimental setup and data processing methodology are presented. Qualitative and quantitative results from each measurement location are discussed along with uncertainties to explain certain key flow physics. Additionally, skin friction coefficients from selected overlapping measurement locations from another experimental flow measurement technique called Laser Doppler Velocimetry (LDV) are compared with OFI, and a cross-instrument study is performed. Finally, results from well-refined RANS CFD simulations are assessed with the experimental results, and critical improvement areas are identified.

I. Nomenclature

C_f	=	Coefficient of skin friction
H	=	Height of the hill
h	=	Height of the oil film
t	=	Time

*Graduate Researcher, Department of Aerospace and Ocean Engineering AIAA Student Member.
†Graduate Researcher, Institute of Aerospace Studies, AIAA Student Member.
‡Graduate Research Assistant, Department of Aerospace and Ocean Engineering, AIAA Student Member.
§Graduate Research Assistant, Department of Aerospace and Ocean Engineering, AIAA Student Member.
¶Graduate Researcher, Department of Aerospace and Ocean Engineering, AIAA Student Member.
‖Graduate Researcher, Department of Aerospace and Ocean Engineering, AIAA Student Member.
**Research Associate Professor, Department of Aerospace and Ocean Engineering, AIAA Member.
††Professor, Department of Aerospace and Ocean Engineering, AIAA Associate Member.
‡‡Professor, Department of Aerospace and Ocean Engineering, AIAA Associate Member.
§§Research Associate, Department of Aerospace and Ocean Engineering, AIAA Associate Member.
¶¶Professor, Department of Aerospace and Ocean Engineering, AIAA Associate Member.
***Professor, Institute of Aerospace Studies, AIAA Associate Member.

τ,τ_w	=	Wall shear stress
μ	=	Oil viscosity
θ_i	=	Angle of incidence of light
ϕ	=	Phase difference
λ	=	Wavelength of light
n_a and n_f	=	Refractive indices of air and oil respectively
Re_H	=	Reynolds number based on height
p	=	Pressure
T	=	Temperature
n	=	Distance between limiting streamlines
q	=	Dynamic pressure
u_τ	=	Friction velocity
w	=	BeVERLI hill base width
$\|S_{i,if}\|$	=	Spatial frequency of interferogram
ρ_{xy}	=	Strength of correlation curve
s	=	Length of an analysis line
x, y, z	=	Tunnel cartesian coordinates

II. Introduction

DRAG reduction is one of the most important factors contributing to increasing transportation vehicles' efficiency. When it comes to aerospace industries, commercial and military aircraft companies emphasize drag reduction since this directly translates to lower fuel consumption. These aircraft, which mostly cruise at subsonic speeds in the high-altitude regions, experience more viscous drag than pressure drag [1]. While there are multiple efforts to measure pressure drag quickly and accurately, more work needs to be done comparatively to make skin friction measurements robust. The turbulent behavior of specific complex flows discussed in this paper could be understood better using accurate skin friction measurements. Laser-based interferometry has been in place since the late 20th-century [2, 3], but this method has proved to be very tedious for covering an entire flow-field. Recently, Oil Film Interferometry (OFI) has been adopted to estimate skin friction more accurately and effectively for complex flow geometries [4–10].

The OFI measurement technique has been used in the current study on the NASA/Virginia Tech BeVERLI (**Be**nchmark **V**alidation **E**xperiment for **R**ANS and **L**ES **I**nvestigations) hill model case. BeVERLI hill project is an ongoing benchmark study primarily studied at Virginia Tech [11, 12]. The project focuses on obtaining accurate and detailed experimental data to successfully validate various computational models based on a list of completeness criteria developed by Oberkampf and Smith [13]. This project has now expanded with many other collaborators showing interest in this benchmark study, including the University of Toronto Institute of Aerospace Studies (UTIAS) and SINTEF Ocean who also have been working on similar experiments in parallel. The French National Institute for Scientific Research (CNRS), University of Melbourne, University of Brunswick and Maritime Research Institute Netherlands (MARIN) have been working on computational studies [14, 15].

The purpose of choosing this specific hill model was due to its curved design that contains different flow regimes - the attached flow region, the region where the flow begins to separate, and the turbulent separated regions. Such complex flow phenomenon proves to be a challenging case study for Computational Fluid Dynamics (CFD) turbulence models to predict. Similar benchmark studies have already been carried out by many researchers such as those by Byun [16, 17] and Simpson et al. [18] and by Bell et al.[19] on axisymmetric hill models, but none of these studies could document and discuss the high experimental completeness level of the database required to validate CFD models [13]. The main objective of this project is to obtain a high completeness level by measuring the complex three-dimensional flow over BeVERLI hill through various flow measurement techniques such as Particle Image Velocimetry (PIV), Laser Doppler Velocimetry (LDV), Oil Film Interferometry (OFI), fluorescent oil flow visualization and static pressure measurements. Preliminary results from the experiments at Virginia Tech, SINTEF, UTIAS, and computational results from all the various collaborators have already been discussed in multiple research articles [14, 15, 20, 21].

This paper mainly discusses the OFI measurement technique implemented at Virginia Tech. The skin friction coefficient (C_f) estimates were obtained at three Reynolds numbers for multiple locations on the BeVERLI hill. Collaboration with UTIAS played a crucial factor in the successful execution of the OFI technique at the VT Stability Wind Tunnel (SWT). The experimental setup for these measurements, including the various challenges involved in capturing high-quality fringe images and the camera calibration methodologies specific to this experiment, are discussed

in detail. Fringe images were processed using a modified version of the code by Naughton [22], and an example analysis is provided for clarity. C_f results from all the measurement locations are presented qualitatively and quantitatively through raw image comparisons and bar plots to better understand the flow physics around the hill. Results from all the overlapping measurement locations from LDV are compared with OFI. Finally, experimental skin friction coefficient results are compared with the results from a RANS CFD simulation to achieve a partial CFD validation.

III. Experimental Setup

A. Stability Wind Tunnel

The experiments for this project were conducted at the Virginia Tech stability wind tunnel operated by the department of Aerospace and Ocean Engineering (shown in Fig. 1). The facility has a rectangular test section of dimensions 7.3m x 1.83m x 1.83m, is a closed-circuit wind tunnel that can generate a maximum speed of 80m/s in the test section which translates to about 5 x 10^6 Reynolds number per meter. The flow in the test section maintains very low freestream turbulence values that range between 0.016% to 0.031%. The test section has two interchangeable chambers for testing aerodynamics and aero-acoustics, and for this study, a hybrid anechoic chamber with modular hard walls [23, 24] was used. Such a design offered flexibility in model mounting and instrumentation access to obtain multiple flow measurements. The BeVERLI hill model was mounted on an aluminum plate on the port side wall of the modular test section, as shown in Fig. 2. A local Cartesian coordinate system was defined relative to the center of the hill, with the x-axis aligned to the streamwise direction.

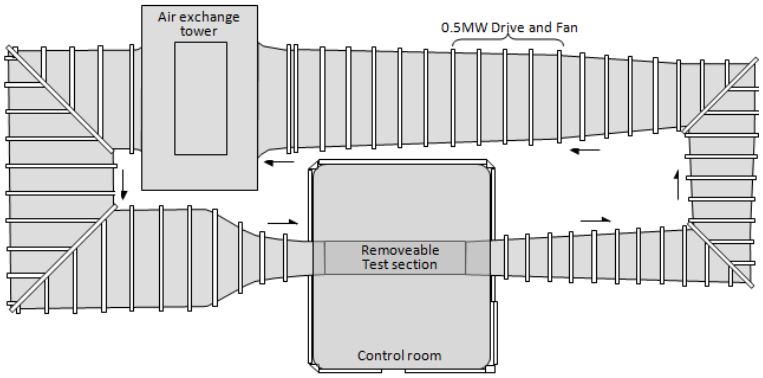

Fig. 1 Schematic of the Virginia Tech stability wind tunnel detailing the features of the removable and closed circuit test section.

B. BeVERLI Hill Model

The BeVERLI hill model is a smooth parametric geometry formed by an extruded 5th-degree polynomial center-line curve with super-elliptic corners. Dimensional specifications of the BeVERLI hill are shown in Fig. 3 [11]. It has a maximum height of $H = 0.1869$ m and width of $w = 0.9347$ m, with a flat top square of width 0.093 m. The model was manufactured using a CNC machine with high-density epoxy foam as the base material. It was then spray painted black, after which a clear glossy coat was added. The purpose of having a glossy black finish on the entire hill was primarily for OFI measurements since high reflective surfaces aid in capturing good-quality fringe images. The article by Naughton discusses surface requirements for OFI measurements in detail [5].

The hill model has four windows along the center-line curvature, with two adjacent windows fitted with anti-reflective clear acrylic panels for LDV measurements. The other two windows were fitted with similar acrylic panels but coated with the same finish of the black paint as that of the surface of the Hill, is shown in Fig. 4. These two windows were the primary measurement locations for OFI. While it would have been ideal to obtain OFI measurements across the entire hill surface, camera calibration was a challenge on the 3D curves. Additionally, the hill was designed to demonstrate rotational symmetry at every 90° yaw angle. For this study, all the measurements were taken at a yaw angle of 45° with respect to the inflow direction, as shown in Fig. 4.

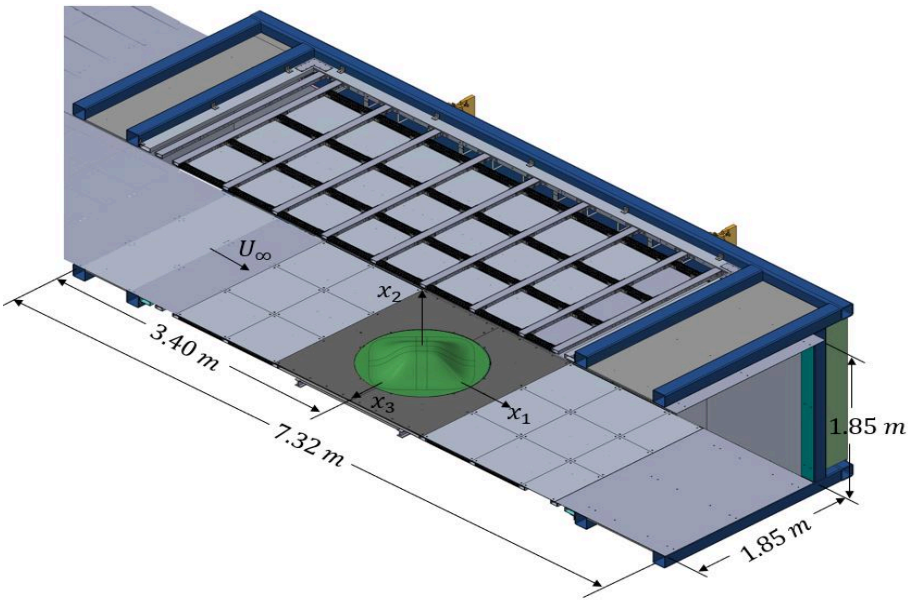

Fig. 2 Detailed Specification of the BeVERLI Hill model at the test section of the Virginia Tech Stability Wind Tunnel.

IV. Oil Film Interferometry

A. Background Theory

Thin oil streaks when, subjected to shear stresses due to airflow, form thin sheets of oil with height-to-length ratios of magnitudes more than 10,000. The formation of thin sheets is generally due to wall shear stresses, surface tension, gravity, and flow pressure. However, the most dominant force driving this technique is the wall shear stresses, and all other influencing parameters can be negligible and ignored. Eq. (1) is the thin oil film relationship [4] and is represented as follows -

$$\frac{\partial h}{\partial t} + \frac{\partial}{\partial x}\left(\frac{\tau_{w,x} h^2}{2\mu}\right) + \frac{\partial}{\partial z}\left(\frac{\tau_{w,z} h^2}{2\mu}\right) = 0 \tag{1}$$

$$h = \frac{\lambda\phi}{4\pi}\left(\frac{1}{\sqrt{n_f^2 - n_a^2 sin^2\theta_i}}\right) \tag{2}$$

$$C_{f,i+1}^{0.5} = \frac{\int_0^x (n/C_{f,i})^{0.5} dx}{h\sqrt{n}\int_o^t (q/\mu) dt} \tag{3}$$

$$C_{f,1} = \frac{\mu x}{qht} \tag{4}$$

Eq. (1) describes the evolution of the height of the oil layer in time when subjected to shear stress. The thin nature of the oil film was perfect for using an interferometry technique, and along with using a monochromatic light source, oil height could be estimated, which was first proposed by Tanner and Blows [25] in 1976. A detailed explanation of the theory and principle of OFI, along with the importance of constructive and destructive interference patterns is explained in Naughton et al. [6, 26]. Thus, the height of the oil film can be calculated using Eq. (2), which is a formulation of certain optical quantities - phase difference, refractive indices, and light incidence angle. Estimation of phase difference (ϕ) was performed using an FFT approach which will be explained later in this paper. Light incidence angle was determined from the camera calibration step, while the refractive indices of air and oil were known quantities. Galerkin and Ackman [27] proposed a modified iterative version of the thin oil film equation which directly estimates the skin

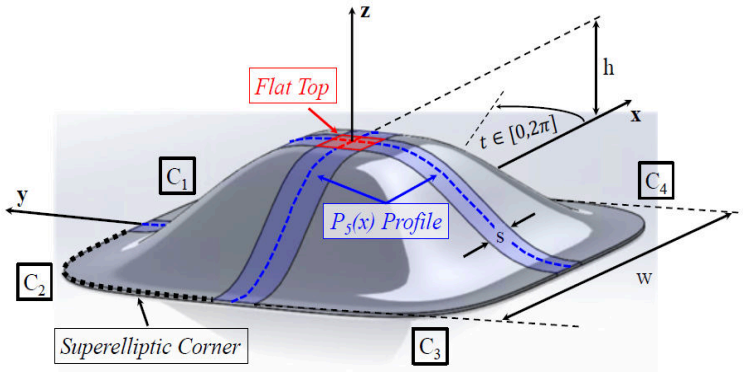

Fig. 3 Dimensional specification of the BeVERLI Hill detailing the 5th degree polynomial profiles and the flat top regions [11].

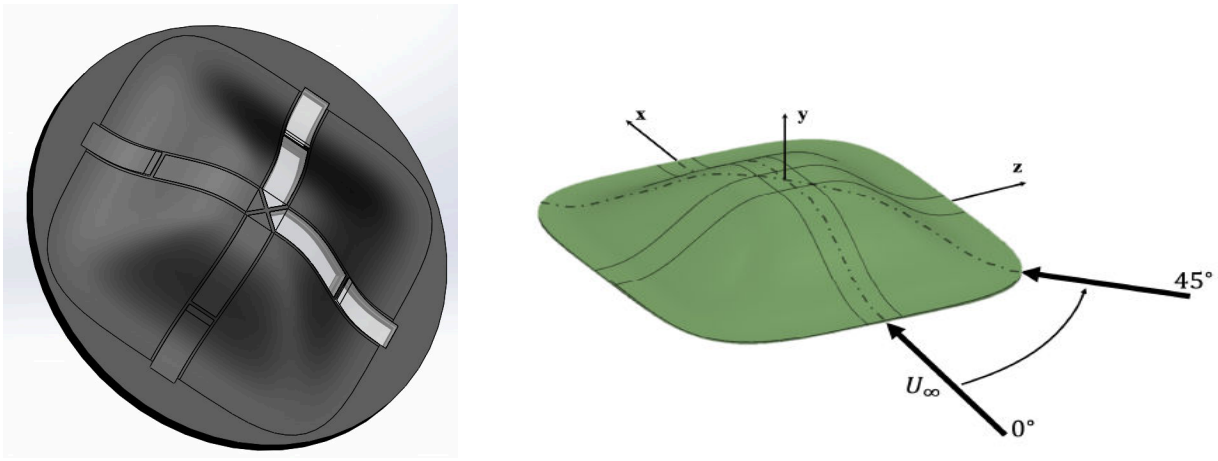

Fig. 4 As-manufactured LDV-OFI BeVERLI hill model (left) showing the two types of windows and a representative figure of the 45° yaw angle of the hill with respect to the inflow (right) [14].

friction coefficient through Eq. (3). This version of the equation requires prior knowledge of streamlines determined either through oil flow visualization or through a CFD solution. Time-integrated values of dynamic pressure and oil viscosity were also required. Finally, an initial guess in the form of Eq. (4) was required in Eq. 3 to calculate a constant shear stress solution.

B. OFI Setup and Specification

The OFI instrumentation setup used for this study consisted of two low-pressure sodium vapor lamps, each powered by two 18W bulbs, silicone oils of varying viscosities, and a high-resolution mirror-less digital camera. The Setup apparatus also included two custom made 0.6m x 0.6m aluminum panels with clear acrylic windows and support structures to hold lighting and imaging equipment, a sharp foam putty knife for applying thin streaks of oil, and white contact papers for light diffusion. As discussed previously, the surface finish on the BeVERLI hill was smooth and reflective to capture high quality fringe images. It was of this nature as a smooth reflective surface was ideal for generating visible interference patterns between air, oil, and the hill surface [5]. The setup configuration used for the BeVERLI tests followed one of the four suggested specifications proposed by Driver [7].

The sodium vapor lamps, each consisting of 18W Philips bulbs [28] were positioned on a modified acrylic window panel on either side of the hill. The OFI measurement technique captures interferograms generated by very thin oil films which do not require light sources with long coherence length and hence a non-coherent light sources, such as the sodium vapor lamp, were ideal. Sodium vapor lamp is monochromatic and has a wavelength of 589nm, which

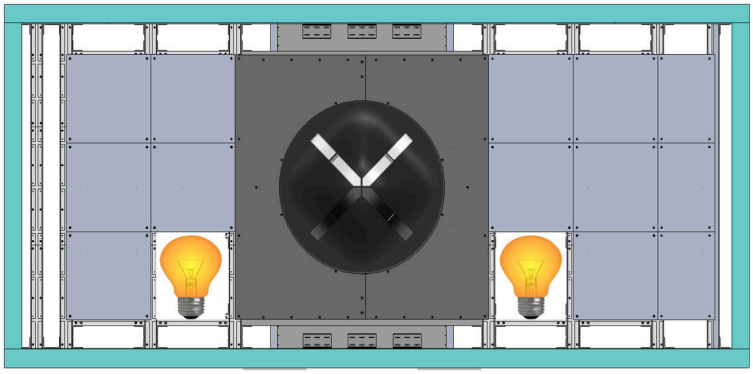

Fig. 5 Positioning of the sodium vapor lamps along the either side of the hill in the VT SWT test section.

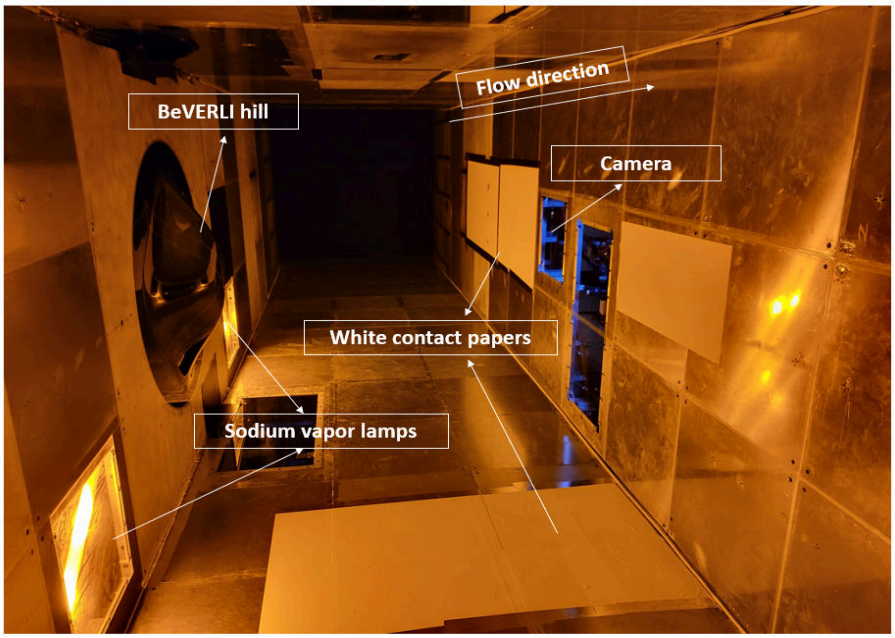

Fig. 6 OFI measurement system implemented at the VT Stability wind tunnel showing all the essential instruments before a test run.

eliminates any speckles that lasers or similar light sources would otherwise create. Additionally, the setup and operation costs of the lamp were straightforward and cheap. The strategic positioning of the lamps was to ensure that the light was not focused directly on the hill, but instead was diffused uniformly within the test section with the help of white contact papers. The matte white contact paper was applied on the other three walls of the test section, as needed to create a uniform reflective screen on the measurement location and serve the purpose of light diffusion. A schematic representation of the light positioning at the VT SWT test section is shown in Fig. 5.

A Sony Alpha ILCE-6500 mirrorless camera body [29] was used to capture the fringe images. It consists of an APS-C type imaging sensor of dimensions 23.5 x 15.6mm and an effective resolution of 24.2 megapixel. It also features the capability of being driven remotely from a mobile application or a laptop with an HDMI cable connection. Remote camera control proved extremely time-saving during the test runs and avoided frequent physical contact with the camera. A high-resolution Sony telephoto zoom lens with a variable focal and aperture range of 70-300mm and 4.5-5.6, respectively, was used along with the camera body. The reason for using a lens with such a large focal length was due to the large width of the test section and the small size of a measurement region. The camera system was mounted on a custom made acrylic panel for quick transitioning of camera positions on the starboard wall based on the measurement

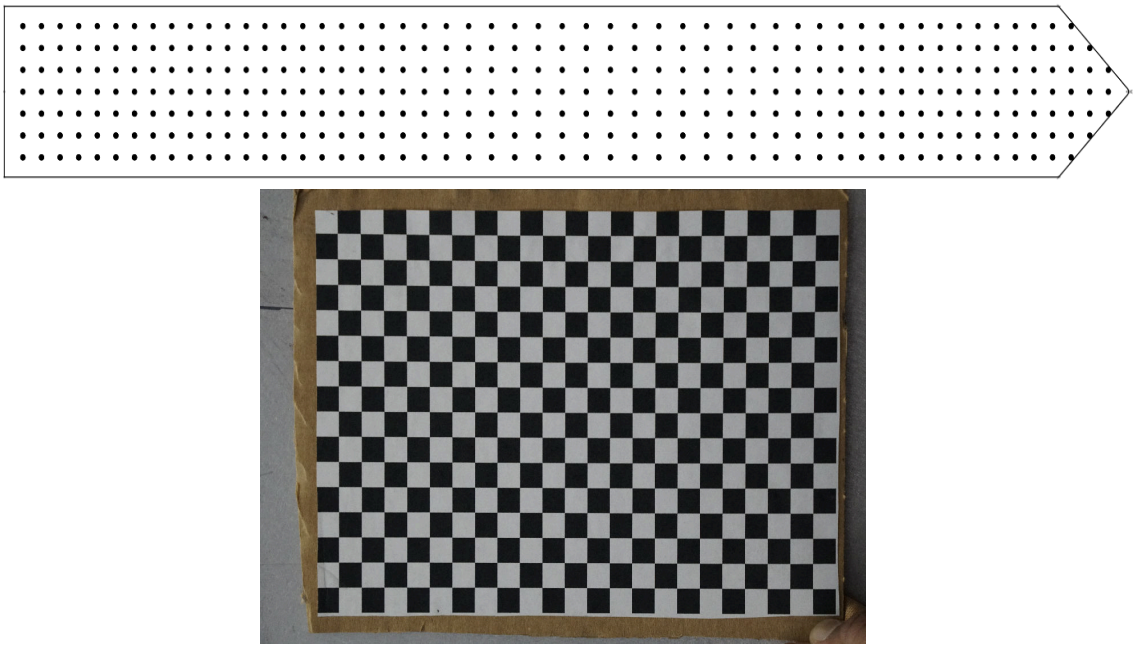

Fig. 7 Dot grid calibration sheet in the shape of the OFI window (top) with a spacing of 10mm between the dots and checkerboard calibration board (bottom) with 10mm squares.

locations. The complete OFI measurement system implemented at the VT SWT is shown in Fig. 6.

Clearco Polydimethylsiloxane Fluid [30], also commonly known as PDMS pure silicone oil was used to initiate fringe generation. The oil is a clear, odorless, colorless linear fluid known for its low viscosity variation with temperature. The oils were calibrated to their corresponding viscosity by the manufacturer at 25°C. Detailed specification of oils are discussed in reference [30]. For this project, oil viscosities of 20cSt, 50cSt, and 100cSt were used, and applied at each measurement location as thin streaks using a sharp edged putty knife. Finally, the camera calibration procedure included a two step process for which two different calibration patterns were printed on a sheet. For the first step, which is the intrinsic calibration of the camera properties, a checkerboard pattern was used with a checker width of 10mm. For the extrinsic calibration process, which was done for mapping the physical and pixel coordinates, a dot grid pattern was generated using a Matlab code to follow the shape of the OFI window. Each dot was spaced 10mm apart in horizontal and vertical directions. The distortions created due to the 5th degree polynomial curve of the windows were accounted for when generating these dots in the Matlab code. The checkerboard and the dot grid patterns used in this experiment are shown in Fig. 7.

C. Processing Methodology with an Example Analysis

Images from the OFI measurements were processed using the Matlab code developed by Naughton [26] and Liu [31]. The first step in the analysis procedure was to complete camera calibration using the checkerboard and dot-grid images collected before each run. Next, the code processed the run conditions that were used to compute skin friction results. The user then defined a set of analysis lines that extend over the fringe patterns in the collected images where skin friction results were desired. After this, the code assisted the user through identifying locations of local peak pixel intensity for each light and dark band of the fringe pattern along each analysis line. For the selected locations along each line, the oil-film height was then determined using Eq. (1), and the corresponding skin friction was calculated using Eqs. (3) and (4). The complete steps involved in the OFI data processing methodology can be seen in the flowchart Fig. 25

As discussed before, the first step in processing OFI measurements was camera calibration, which operated on the principle of photogrammetry [31]. This step was critical to the overall OFI analysis process as poor camera calibration will result in the inaccurate mapping of pixel coordinates in the images to a three-dimensional model coordinate system. Camera calibration was completed in two parts. The first step was calibration for the intrinsic properties of the camera, and the second was to build the mapping from image pixel coordinates to the physical coordinates of the model. Intrinsic

calibration of the camera was completed using the checkerboard images collected for each run and the Matlab Single Camera Calibrator App [32]. The second part of the camera calibration procedure had the user manually assign a series of dots from the dot-grid image to their corresponding physical coordinate. Using the assigned points and intrinsic and distortion parameters found previously, a mapping for any pixel in the image to physical coordinates was created, as seen in Appendix, Fig. 24. Results from this mapping were used in the remaining steps of the analysis process to convert pixel distances to physical distances and vice versa.

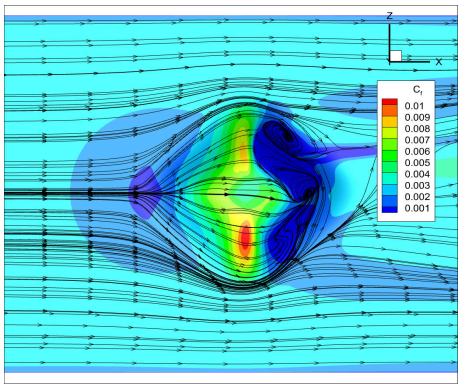

Fig. 8 Streamlines plotted on skin friction coefficient (C_f) contours from RANS k-ω SST CFD results on a level 1 grid that was used in the OFI processing code.

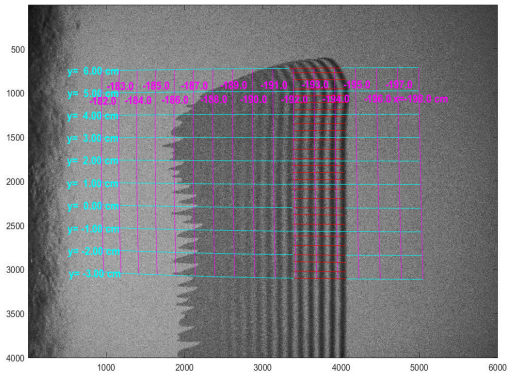

Fig. 9 Analysis lines (in red) generated from local surface streamline mapping extracted from the CFD results.

With the camera calibration steps completed, a set of lines over the fringe image were generated where skin friction results were desired. These lines must follow the local surface streamline of the flow; thus, knowledge of the surface streamlines for the flow was required for the accurate creation of analysis lines. Surface streamline mappings are often extracted from separate oil-flow visualization tests [5]. For this analysis, the surface streamline mapping was generated from CFD simulation results of the same flow over the model, as seen in Fig. 8. The user specified the start location and length of each analysis line. The start location of the analysis line was placed before the leading dark fringe line in the pattern. This ensured that the pixel intensity for the first dark fringe band would be fully captured in the analysis process. The analysis line was then extended for the prescribed length following the surface streamline that passed through the defined start location. Multiple analysis lines were generated using this procedure to generate an average skin friction value, as can be seen in Fig. 9.

FFT was then performed on the image pixel intensity along each analysis line. The peak spatial frequency detected from the intensity pattern was identified, and a corresponding sine wave of the same frequency was generated. A cross correlation was then performed with the pixel intensity signal and the defined sine wave, which can be seen in Fig. 10. The user then selected the local minima and maxima along the correlation curve that were to be removed. The remaining

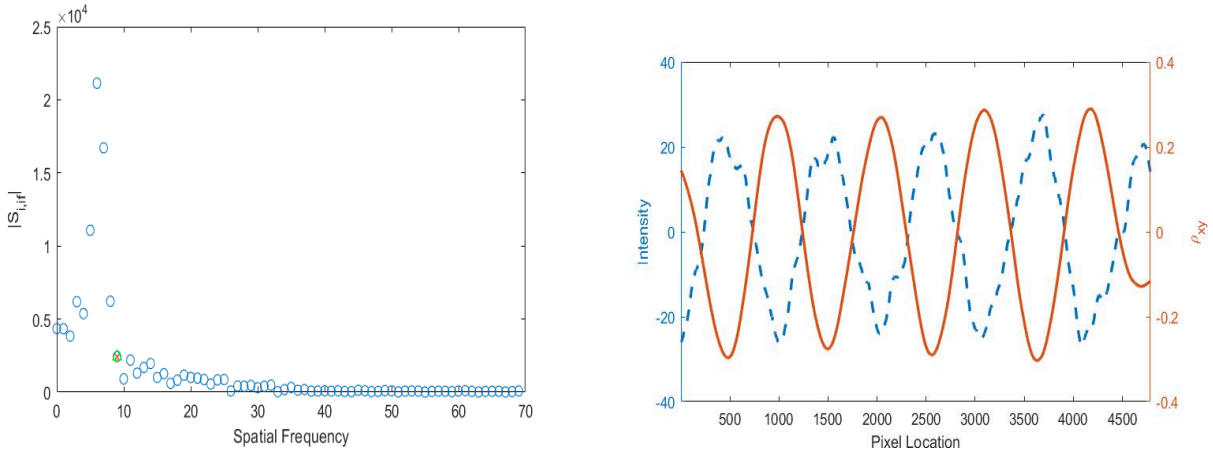

Fig. 10 Peak spatial frequency automatically identified by the code (left) and a sine wave cross correlation curve generated with this frequency and overlapped with the image intensity curve (right).

points were the locations along the analysis line where skin friction results could be computed. The corresponding height of the oil-film, h, was calculated for each of these locations and the leading edge of the oil-film was extrapolated from the calculated film heights. Two limiting streamlines were created by moving a set distance in both directions orthogonal to the plane defined by the model surface normal and the surface streamline at the start location of the analysis line. These two limiting streamlines were created and processed using the same procedure as the original analysis line. The distance between the limiting streamlines, n, was calculated for each pair of similar oil-film heights. Compiling this information, the skin friction coefficient (C_f) at each prescribed location along the analysis line was found using Eqs. (3) and (4). The results from these analysis steps are seen in Fig. 11

D. Uncertainty Quantification

Multiple sources of uncertainty were considered in this study. These uncertainty sources could be divided into two - the systematic and random errors. One major contributor to systematic error was oil viscosity variation, which could occur either from its calibration or due to the inaccuracies in the hill surface temperature measurement. The oil calibration uncertainty was usually very low, and as per the company specifications [30], this was less than 0.2% of the initial calibrated oil viscosity at 25°C. Also, silicone oils are known for their little change in viscosity with temperature [30]. Errors in temperature measurement during the test runs were the major contributor to the viscosity change. The Omega Thermistor type 44004 thermocouple used for measuring temperature was highly accurate and had a measurement uncertainty of ±0.2 K per the manufacturer. However, this instrument was located near the test section entrance, downstream from the hill, and the surface temperature might vary from this thermocouple measurement location. After multiple measurements, the uncertainty was estimated to be 0.28% or roughly ±0.5K. Instrument uncertainties in the measurement of dynamic pressure were also considered. Measurement uncertainties of freestream velocity and atmospheric pressure are ±0.3m/s and ±33Pa, respectively, and using the uncertainty from temperature, errors in dynamic pressure were ±6.6Pa. Wavelength errors from the low pressure sodium vapor lamp was also considered, and they were usually around ±1 nm.

All the different instrument errors were independently assessed by implementing the previously discussed error values in the OFI code. Their subsequent effect on the change in the final value of the skin friction coefficient was quantified. The processing code uses a temperature corrected viscosity, μ_c for estimating C_f and was estimated using the following equation,

$$\mu_c = \mu_o 10^{\left(\frac{C1}{273.15 \pm \partial T} - \frac{C1}{T_c + C2}\right)} \tag{5}$$

where T_c is the temperature at which the oil was calibrated, μ_o is the viscosity of the oil at the calibrated temperature T_c. C1 and C2 are constants for the calibration curve based on the calculations by Naughton and Sheplak [5]. The final skin friction coefficient value had an average temperature based uncertainty of less than 1.5% for all the cases. The dynamic pressure measurement error of ∂q = ±5 Pa is added to the initial dynamic pressure q_o before time integrating into Eq.

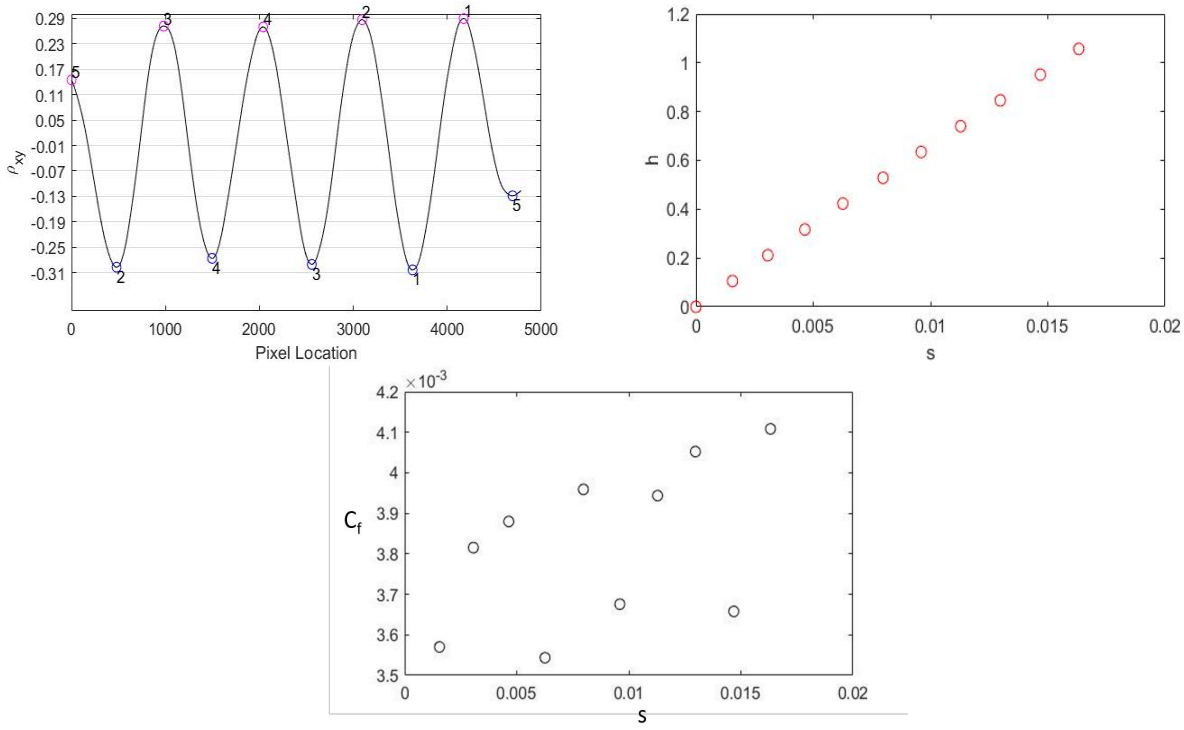

Fig. 11 Local minimum and maximum identified from the cross correlation curve (top left) and height of the oil curve calculated and plotted along the length of the fringe path (top right). The final image (bottom) shows the skin friction co-efficient, C_f results along a single analysis line.

(4) such that $q = q_o + \partial q$. The error in the dynamic pressure measurement had an uncertainty of 0.7% in the final C_f values. Additionally, the wavelength error from the sodium vapor lamps contributed only about 0.22% uncertainty to the final C_f values. Thus, the average systematic errors in C_f were less than 3%.

Random or precision uncertainties usually occur due to factors such as uneven surface finish, image distortions/noise generated because of vibrations in the test section, poor fringe image due to the influence of cellophane tape, or poor visibility of the fringes from reflections and shadows near the measurement region. Such type of errors can be reduced by taking multiple samples. In this study, they were reduced by evaluating C_f along many analysis lines in a single measurement location/fringe image. Usually, the number of analysis lines evaluated per measurement location was around 15 to 20 to yield at least 10 independent C_f values per analysis line. This led to a total of at least 150 to 200 C_f values extracted from a single measurement region. These C_f values were then averaged to obtain a single value. The method of reducing random errors by taking many samples along the same region or by adding more analysis lines in a fringe image was discussed by Naughton et al.[6, 26] and [33].

Errors could also occur due to the nature of the OFI processing code, which requires a skilled researcher to perform the analysis process. Human errors can be evaluated by independently analysing the same image from a measurement location by two different skilled researchers and accounting for the difference in the C_f values obtained between them. The error from this source was usually less than 0.5%. Errors from non-consistent run conditions, such as start up and shutdown uncertainties, were not evaluated in this study. However this should generally be very low since this was usually less than 5% of the total run time. Tunnel shutdown time will not cause uncertainty in this study since all the images were captured while the tunnel was running. Gluzman et al. [33] mentioned that their start up and shut down error was only about 0.7% of their total uncertainties for a startup and shutdown time was about 3.33% of the total run time. Finally, location uncertainty from the photogrammetry procedure employed in this study was very low and was usually less than 10 pixels which, when converted to physical distance, was less than ±0.2mm.

V. Results

Skin friction coefficient results from 13 different test locations on the hill and on flat panels in the inflow regions of the hill will be discussed in further sections. Various aspects such as flow visualization, Reynolds number effects, separation regions, and C_f comparisons with other flow measurement techniques are explained. The different measurement regions on the hill are shown in Fig. 12, and their corresponding coordinate ranges are available in Table 1. These regions were split into two, namely - inflow and wake regions, and measurements were taken at three different Reynolds number based on the height of the hill - Re_H = 250,000, 325,000, and 650,000. Each experiment was set up such that a thin streak of oil was applied at a measurement location using a knife edged putty before ramping up the wind tunnel. Oil viscosity of 20cSt was used for the $Re_H = 250,000$ and $325,000$ cases while 100cSt oil was used for the $Re_H = 650,000$ cases. After applying the oil at the desired location, the wind tunnel was ramped up to its respective Reynolds number. During this step, flow conditions required for post-processing data were output from the data acquisition system. Flow conditions data file consists of time series data of freestream velocity, dynamic pressure, temperature and time stamp. During a test run, multiple fringe images were captured with a digital camera operated through a computer. The images, the run conditions data file, and the calibration images were then transferred to a local hard drive for later post-processing. Generally, one of the last images captured during a test run was used for the analysis process from which the skin friction coefficient was estimated following the steps discussed in Section IV.C.

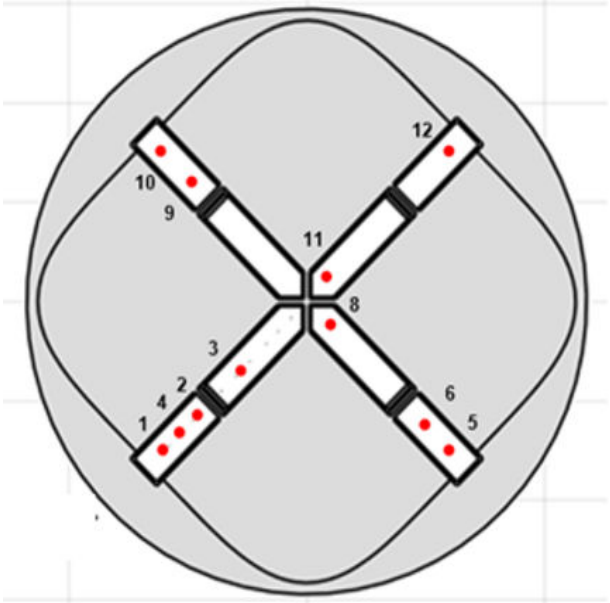

Fig. 12 OFI measurement locations on the BeVERLI Hill.

A. Qualitative Analysis

Fig. 13 shows the images captured at the start and end of a test run at locations 9 and 10 for $Re_H = 650,000$. From these two images, it can be observed that the captured raw images can be used to estimate two parameters qualitatively - flow direction and wall shear stresses. Shear stresses between locations can be compared using the knowledge that fringe spacing increases when the region experiences higher shear stresses. Firstly, to demonstrate the use of the fringe images to determine the flow direction, six fringes from different regions of the hill captured at $Re_H = 650,000$ were considered and are as shown in Fig. 14. These images were arranged to follow the labeling convention in Fig. 12. The images, when viewed together, roughly demonstrate the overall flow direction on the hill and serve as a primitive flow visualisation technique. They also help to capture critical features, such as the attached and separated flow regions. From the images, it can be observed that there are flow deflections due to the hill curvatures. The locations on the upper and lower part of the OFI window labeled 1, 2, 9, and 10 capture these deflections through the fringe image angles with respect to the freestream direction. Flow at regions 8 and 11, which are located near the hill center, has little flow deflection and can be observed to follow the direction of the freestream flow. Flow near region 6, located in the hill's wake region, appears. Flow separation was deduced from the nature of the fringes captured since they were in the

Table 1 Labeling of OFI locations and their nominal coordinate location ranges in tunnel coordinates.

Location	X_1/H	X_3/H
P3M	-10.23 to -10.26	0.16 to 0.29
P4M	-7.10 to -7.15	0.25 to 0.27
1	-1.64 to -1.84	-1.49 to -1.71
2	-1.47 to -1.28	-1.08 to -1.71
3	-0.62 to -0.90	-0.65 to -0.91
4	-1.43 to -1.56	-1.37 to -1.49
9	-1.17 to -1.27	1.13 to 1.41
10	-1.68 to -1.79	1.62 to 1.84
5	1.62 to 1.72	-1.61 to -1.81
6	1.16 to 1.26	-1.20 to -1.34
11	0.22 to 0.35	0.02 to 0.24
12	1.61 to 1.71	1.65 to 1.79

opposite direction of the freestream flow, indicating reverse flow. Results from location 6 serve as a good example of how OFI can be used to determine the separation regions. Flow at regions 5 and 12, located at the window bottom and top corners, respectively, appears to be still attached and continues to follow the hill curvature. Thus, Fig. 14 can be used to understand the hill's local flow directions, which could be further improved by having more measurement locations spread across the hill. Fig. 15 shows the image captured from the oil flow visualisation technique at Re_H = 650, 000. The image generally agrees with the previously discussed flow directions. A higher resolution OFI that spans the entire model surface can thus be used in place of oil flow visualisation, which requires extensive cleaning and the larger quantity of oil.

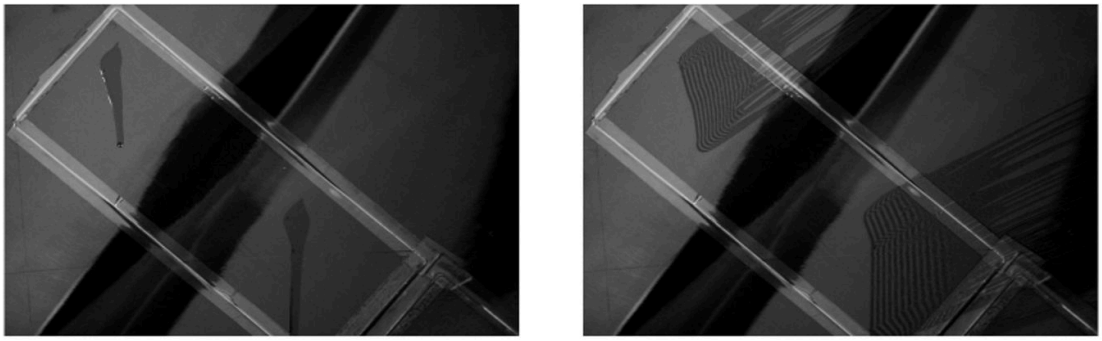

Fig. 13 Fringe images captured before the start of the wind tunnel ramp-up (left) and at the end of a testing(right) at locations 9 and 10 at a Re_H =650,000.

As mentioned, qualitative analysis can also be performed to understand local shear stress variation based on fringe spacing. For the same oil viscosity and average test run time, Fig. 16 shows the fringe development at three locations along the windward side of the hill. From these images, it can be observed that the fringe spacing increases from locations 1 to 3 indicating that the skin friction increased along the OFI window and towards the center of the hill. The increase in skin friction indicates increase to the local in the wall shear stresses and flow velocity. Similar trends were observed at all the other windows. Reynolds number effect on C_f can be qualitatively assessed using the raw fringe images. Fig. 17 shows images captured at the three different Reynolds numbers at locations 1 and 2. Test run time for all three cases was close to ten minutes. The Re_H = 325,000 cases had a larger fringe spacing than the Re_H = 250,000 cases indicating a larger shear stress for the former. The Re_H = 650,000 case, having used a higher viscosity oil, still managed to develop fringes with a spacing similar to the other two indicating large surface shear stresses for this case.

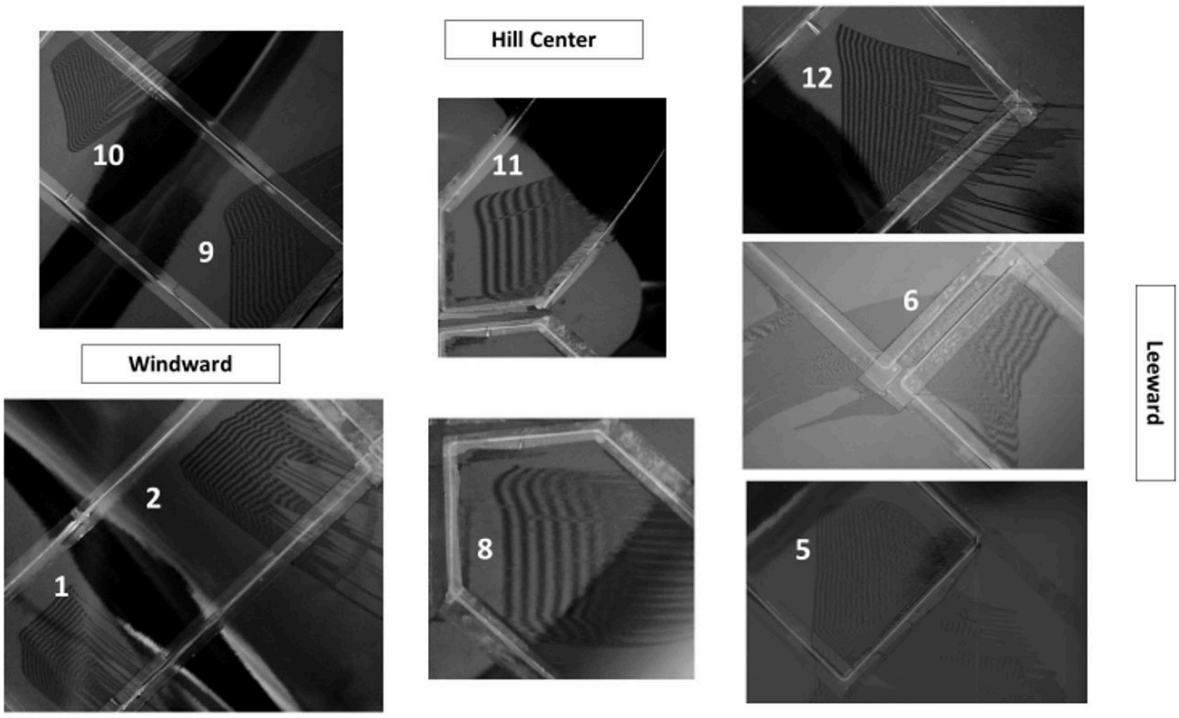

Fig. 14 Concatenation of fringe images at different regions of the hill to be used as a primitive flow visualisation technique.

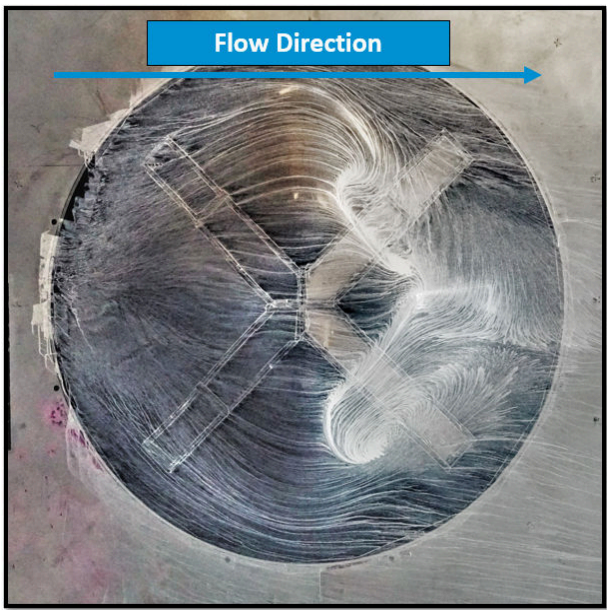

Fig. 15 Image captured from oil flow visualisation at Re_H =650,000.

Finally, Fig. 18 shows the fringes captured near the re-circulation region, which was a good example showing Reynolds number effect on the wall shear stresses. The Re_H = 250,000 cases could not generate sufficient shear stress in the negative flow direction to generate any fringes, but the Re_H = 650,000 cases had sufficient surface stresses for the fringe development.

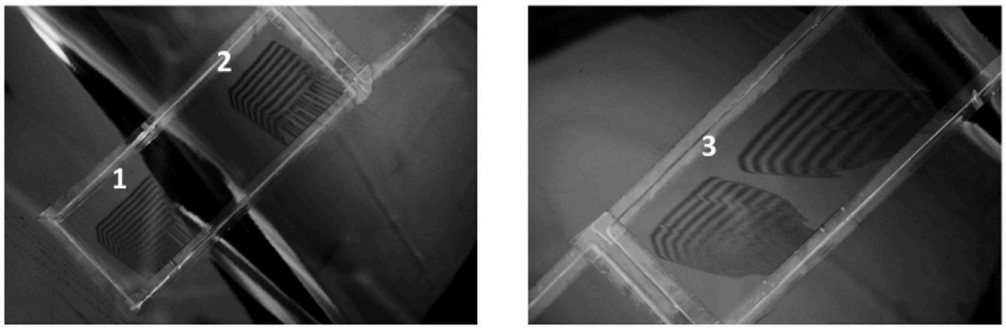

Fig. 16 Qualitative analysis to understand the evolution of skin friction along the OFI window at Re_h=325,000.

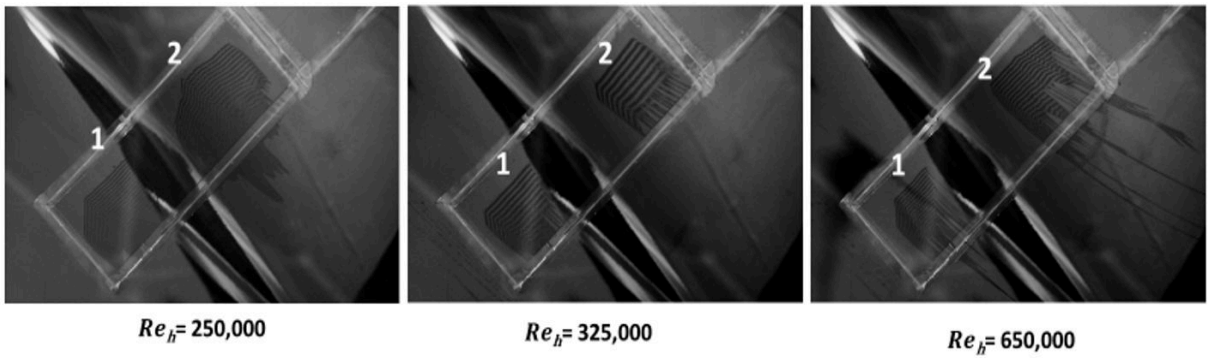

Fig. 17 Reynolds number effects on the wall shear stresses can be qualitatively observed for different Reynolds number based on the fringe spacing.

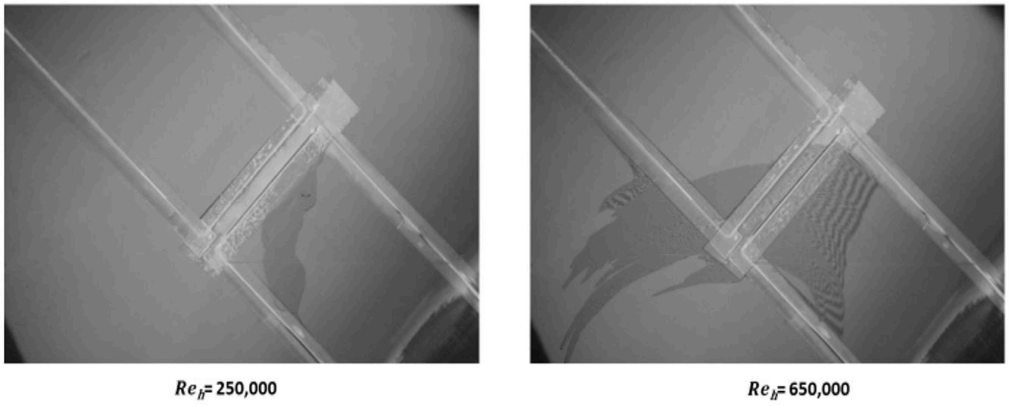

Fig. 18 Raw fringe images that capture the Reynolds number effects on the development of interference patterns in the separation region at location 6.

B. Quantitative Analysis

This section of the paper discusses the C_f results quantitatively which were obtained by processing each image at the measurement locations from the analysis procedures discussed in Section IV.C. These results should complement the qualitative results discussed in the previous section in terms of our estimate of wall shear stress. Averaged skin friction coefficient results calculated from each measurement location are as shown in Fig. 19. The plots are split into three

images for better readability. They consist of results from the locations at windward and leeward regions of the hill, and regions on two flat panels located at a distance of 3 and 5 feet from the hill center. The results were compared among the three Reynolds numbers tested in this experiment. Equations below are essential to note before discussing the results -

$$C_f = \frac{\tau_w}{q_\infty} = \frac{\tau_w}{0.5\rho U_\infty^2} \tag{6}$$

$$u_\tau = U_\infty \sqrt{\frac{C_f}{2}} \tag{7}$$

Eqs. (6) and (7) show that the wall shear stresses are directly proportional to the square of the free stream velocity, while the skin friction coefficient is inversely proportional to velocity. It is also important to note that the free stream velocity is proportional to the Reynolds number, and since C_f and U_∞ are inversely related, C_f should decrease with an increase in Reynolds number. C_f can be used to estimate a near surface flow quantity called friction velocity, u_τ, which is generally required for scaling the boundary layer. Using the above relations and the calculated C_f values, discussions on the near surface flow behaviour can be done. Observing the C_f values from P3M, P4M to location 1, a gradual decrease in its values was noticed along the free-stream direction at all three Reynolds number cases. The C_f reduction was an indication that the surface flow velocity was decreasing as the flow reached the front of the hill. There might also exist a flow stagnation point near this region. C_f values then increase steadily along the OFI window, suggesting that the flow accelerates on the hill curvature regions and might hit a peak local velocity or shear stress somewhere near the hill center. Unfortunately, there was no data at the inflow hill center locations to prove the existence of this phenomenon. Similar trends were observed at locations 9 and 10 with respect to increasing C_f in the direction of the hill center. Measurement locations 1, 2, 9, and 10 were nearly symmetric points along the horizontal axis, which helped to understand flow symmetry at the inflow region of the hill. The upper location regions 9 and 10 predicted higher C_f values when compared to the ones at the bottom window 1 and 2. Flow should ideally be symmetric at these locations due to the symmetric shape of the hill, but this difference in the C_f measurement signifies some possible measurement error at location 9 where a large discrepancy can be observed. The measurements in the inflow regions for the $Re_h = 650,000$ case have closer C_f values at the symmetry points, proving the symmetric nature of the inflow. The measurement error at location 9 could be due to various factors, such as the measurement points not being exactly symmetric or due to the influence of any external disturbances such as from the tape used to seal the window edges. The OFI code makes use of streamlines data from CFD, and at location 9, CFD could be wrongly predicting the flow direction. Another possibility could be due to the manufacturing inaccuracies of the hill.

As the flow advances to the hill top at location 11, located on the leeward side, a high C_f value was observed for all the Reynolds numbers. The coefficient value at this location was slightly lower than that at location 3 from the windward region, suggesting that the accelerating flow could have hit a peak shear stress near the hill center and as it entered the wake region, the flow was starting to decelerate. The flow was probably also going to separate from the hill beyond location 11. Location 6 was a point in the separation region that was earlier identified from the qualitative analysis. From the quantitative analysis for location 6, a low C_f was predicted and that too for the $Re_h = 650,000$ case only since there were no sufficient surface forces for fringe development at lower Reynolds numbers. Locations 5 and 12 were the near symmetric points with respect to the horizontal axis on the leeward region of the hill. These two points can be assessed for flow symmetry on the leeward side using. Location 12 predicts a higher C_f value than location 5 for all three Reynolds number cases, once again suggesting larger shear stresses and skin friction on the upper side of the hill. Recalling the results from inflow hill regions, larger shear stresses were also observed in the upper regions. It was impossible to obtain data at regions between locations 11 and 12 due to time constraints at the time of testing. Thus, no flow symmetry/asymmetry discussion could be made regarding flow separation. One last observation regarding skin friction coefficient variation with Reynolds number can be made from Fig. 19. It shows a general decreasing trend of C_f for increasing Reynolds number and successfully satisfying Eq. (6).

C. Comparison with Other Flow Measurement Techniques

C_f results at certain locations of the hill were compared to the results from another flow measurement technique called LDV. LDV was used to measure the turbulent boundary layer on the hill surface. This technique makes use of doppler shift from microscopic particles passing through the intersection of two or more lasers to measure velocity in fluids. During testing, three overlapping locations between OFI and LDV were identified and independent measurements were taken for a cross-instrument study. The C_f values from LDV for these three locations were computed from the results via a Spalding fit to the data in the linear sublayer. This allowed for the incorporation of nominal wall-height

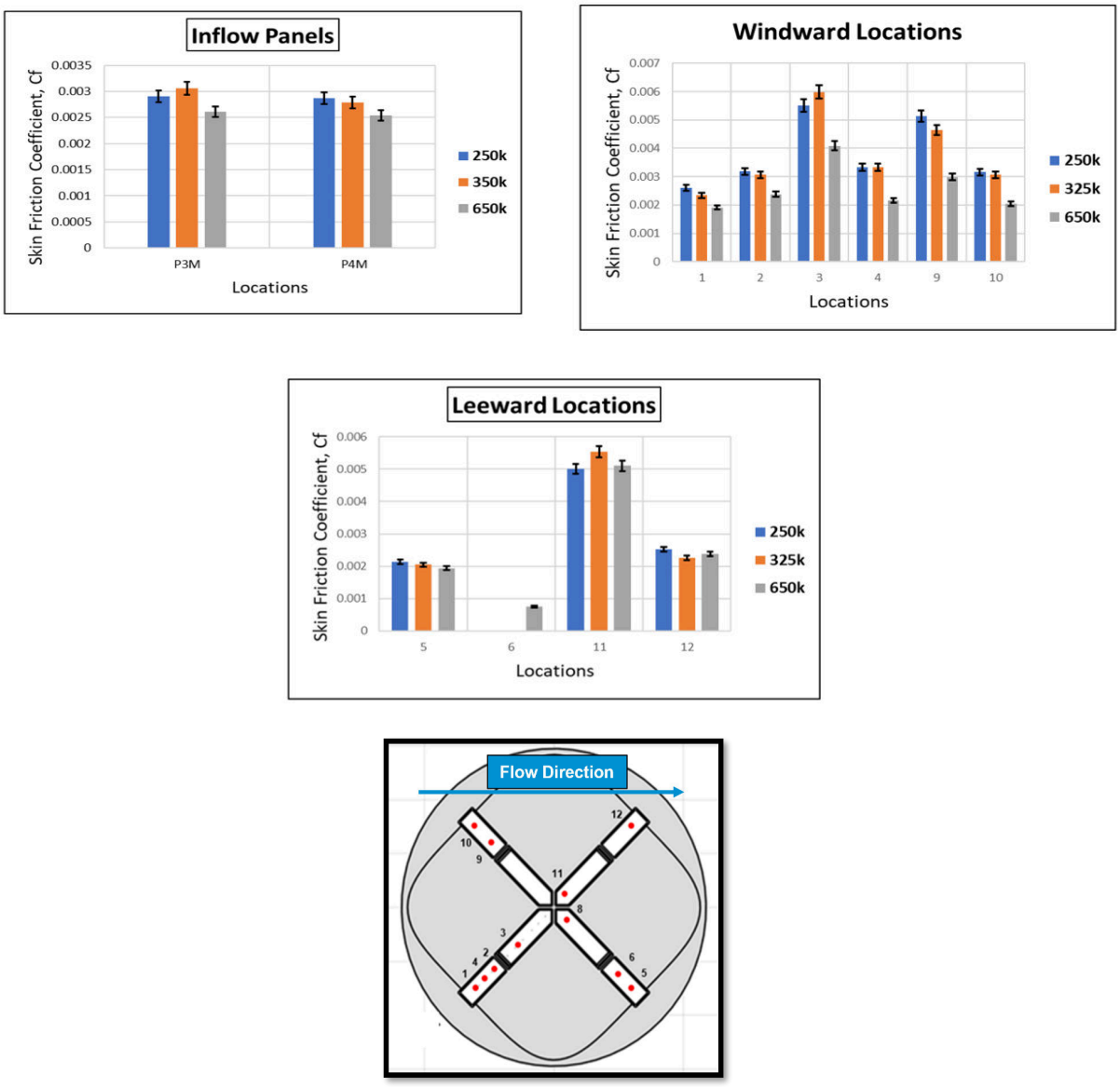

Fig. 19 Skin friction coefficient (C_f) results at all the different measurement location and at the three Reynolds numbers.

corrections to the measured data [34]. The best fit u_τ and y correction were assessed from this fit and applied to the data. u_τ was then transformed to C_f using Eq. (7). These values were then compared with the averaged C_f values from OFI. This data comparison is shown in Fig. 20. Note that the LDV location terminology was different from that of OFI. Locations 2, 3 and 4 of OFI corresponded to W4, W5 and, W3 of LDV. To avoid any confusions during cross referencing, both these terminologies were included in Fig. (20). The Reynolds number comparisons were limited to the 250,000 and 325,000 since no LDV data was available for the 650,000 case.

In general, LDV skin friction measurements were indirect and were lower than the OFI for all the cases. For the Re_H = 250,000 cases, the average difference between the two data was less than 10%, while for the 325,000 cases, the variation between the data was less than 20%. Overall, the data agreement between the two measurements was good. Out of all the data comparisons available, only two locations, 2/W4 and 3/W5 of the lower Reynolds number case have a common uncertainty region. We could predict that the actual C_f value might lie within this uncertainty region. It

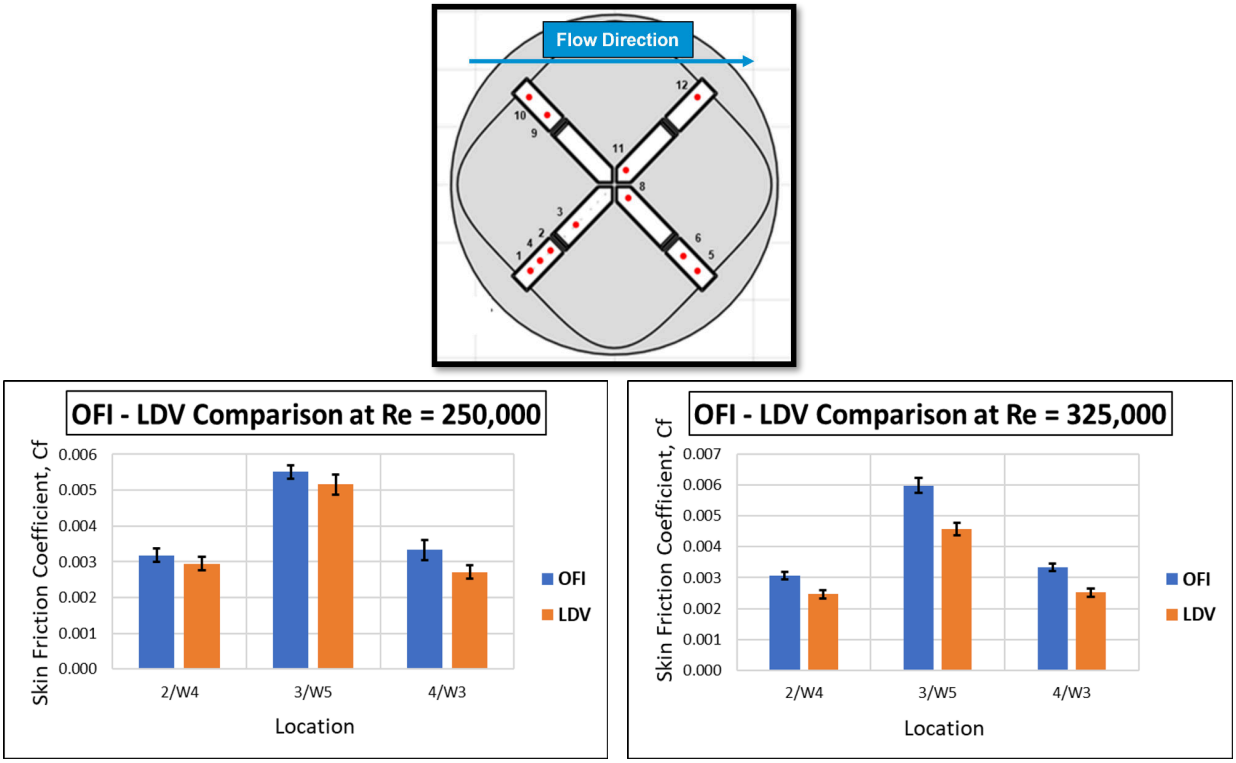

Fig. 20 Skin friction coefficient (C_f) comparison between OFI and LDV measurements at Re_H = 250,000 and 325,000 along with error bars.

was also tough to conclude which of the two measurement techniques was predicting accurate C_f results since various measurement challenges and error sources accompanied both these. Alternatively, OFI measurement of C_f can be used by the LDV measurement technique to easily scale the boundary layer in terms of wall units wherever linear sub-layer measurements were not possible. OFI can also be used to compliment other techniques such as PIV.

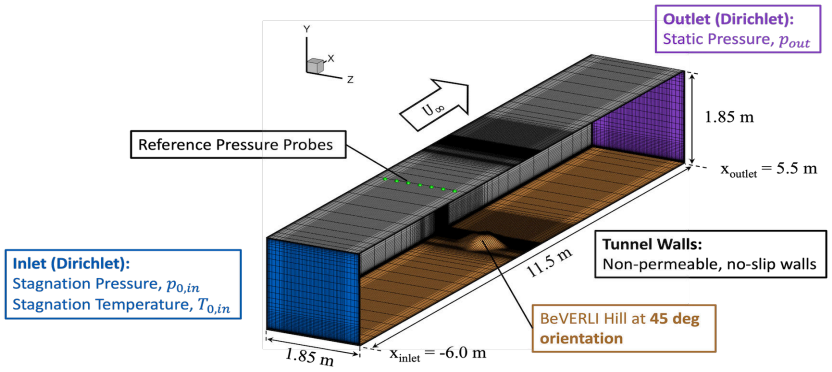

Fig. 21 Computational domain used for the CFD simulations along with the dimensions and details of all the boundary conditions[35].

D. Comparison with CFD

The skin friction coefficient results from OFI contribute to one of this project's main goals, which was to provide detailed experimental data to meet the requirements of CFD validation. A partial CFD validation study was performed

Table 2 CFD Boundary Conditions

$\mathbf{Re_H}$	**250,000**	**650,000**
$p_{0,in}$	94,220 Pa	94,450 Pa
$T_{0,in}$	297 K	297 K
p_{out}	93,961 Pa	92,692 Pa
U_∞	21 m/s	55 m/s
M_∞	0.06	0.16
ρ_∞	1.103 kg/m^3	1.093 kg/m^3
I	0.021%	0.030%
μ_t/μ	1.5	3
p_{ref}	93,974 Pa	92,771 Pa

and discussed in this section. For this validation, C_f results from one of the CFD simulations using a fine grid and a RANS eddy viscosity turbulence model were compared to OFI results. The details of the mesh, boundary conditions and turbulence model are explained in this section. The computational domain used for the CFD simulations was cuboid in shape to resemble the test section at the VT SWT. It extends 6m in the upstream direction of the hill and 5.5m in the downstream direction with an inflow cross-sectional dimension of 1.85m x 1.85m. A system of four structured grids was generated with a refinement factor of $r = \sqrt[3]{2}$ such that level 4 was the coarsest grid and level 1, the finest grid. Level 1 grid was used for this validation which consisted of about 75 million elements of dimensions $557 \times 353 \times 385$ elements. The grids were refined to have a higher density of nodes around the hill and account for the boundary layer on all the walls. A schematic representation of the domain and the grids is shown in Fig. (21). C_f data comparisons were made only with the results from Re_H = 250,000 and 650,000 cases. Detailed specifications of the boundary conditions [35] defined at the inlet and outlet for these two cases are shown in Table 2 and Fig. (21). Ideal, compressible air flow condition was used with Sutherland's viscosity model. Adiabatic and no slip wall boundary conditions were defined on all the other walls. The data used for this comparison was extracted from a RANS case that was simulated in a commercial code, ANSYS Fluent using the Mentor k-ω Shear Stress Transport (SST) turbulence model.

Fig. 22 shows the averaged C_f values from OFI and CFD compared at their respective coordinate locations. C_f values from CFD results were obtained by plotting their contours in Tecplot and probing to the corresponding coordinate locations. CFD under-predicted C_f values of all the OFI estimates at the 250,000 Reynolds number. More significant under-prediction of C_f was primarily observed in the upper inflow regions of the hill at locations 9 and 10. Also, skin friction coefficient results from CFD cases seem to predict a closer symmetrical inflow when observing C_f results at the points of symmetry (i.e., 1, 2, 9 and 10) than OFI. OFI, on the other hand, estimated larger C_f values at the upper inflow locations, particularly at location 9 showing some signs of measurement error at this point. As discussed previously, there was no OFI data available for this Reynolds number in the separation region at location 6; hence, no appropriate comparisons with CFD could be made. CFD does seem to predict a very low C_f value at location 6, which could be due to the presence of the recirculation region at this point. Finally, symmetry points (i.e., location 5 and 12) on the leeward hill side predicted very similar C_f values to OFI, signifying flow symmetry at the wake region. In general, skin friction coefficient variation trends across the inflow and leeward regions of the hill were similar to the OFI measurements.

For the 650,000 Reynolds number case, CFD predictions of C_f were closer to that of the OFI estimates than the previous low Reynolds number cases. Improvements in the agreement between the two data were especially noticed in the inflow regions of the hill. Some variations were observed between the two C_f results in the leeward hill side. From the plots, it can be observed that CFD might be predicting an asymmetric wake with higher shear stresses on the lower leeward side of the hill, while OFI had predicted it on the upper side of the hill. These variations from the CFD results observed at the leeward hill region may be due to the complexity of the flow present here and the current RANS CFD simulations may not capture the flow physics accurately. Finally, C_f comparisons were plotted between OFI, LDV and CFD at the three overlapping locations. Due to the lack of CFD data from the 325,000 case, and the lack of LDV data at the 650,000 case, comparisons were only possible with the lowest Reynolds number case. Fig. 23 shows excellent agreement of the C_f results between the three data sets with variations less than 5-10% among them.

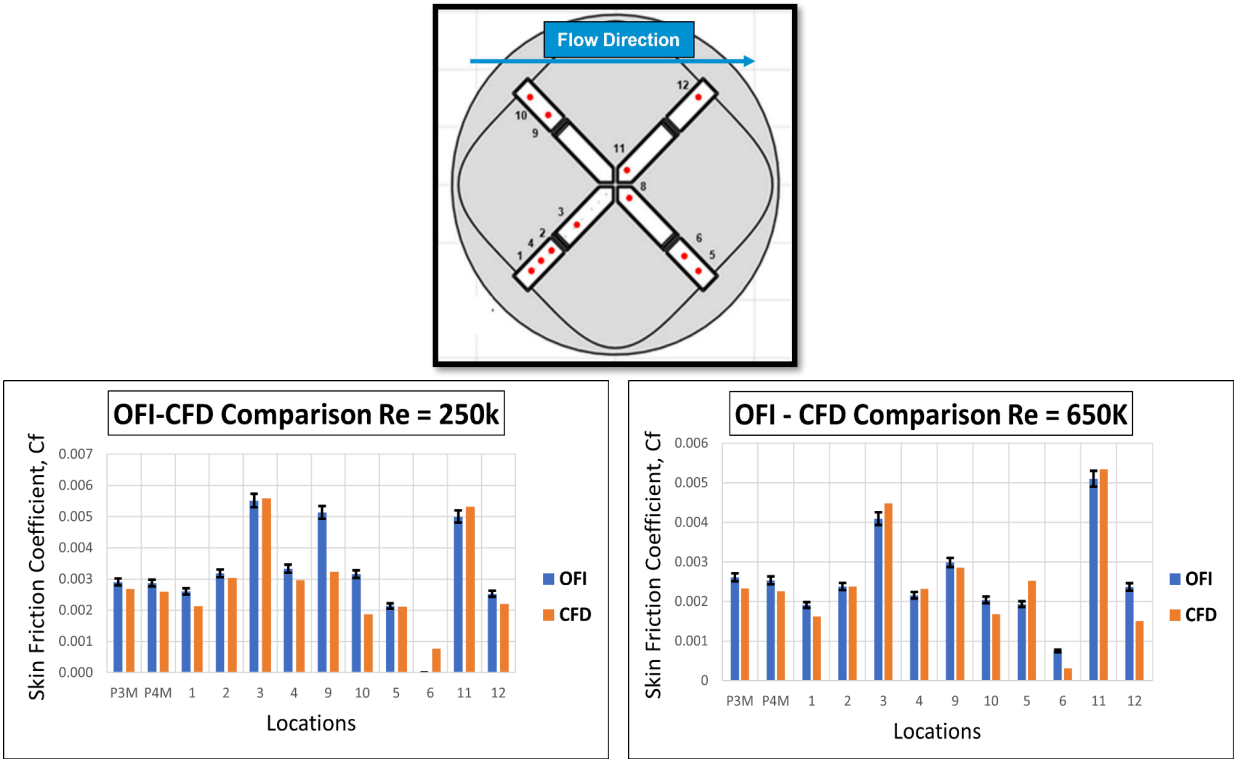

Fig. 22 Comparison of skin friction coefficient (C_f) results between OFI and CFD at all the available OFI locations at Re_H = 250,000 and 650,000.

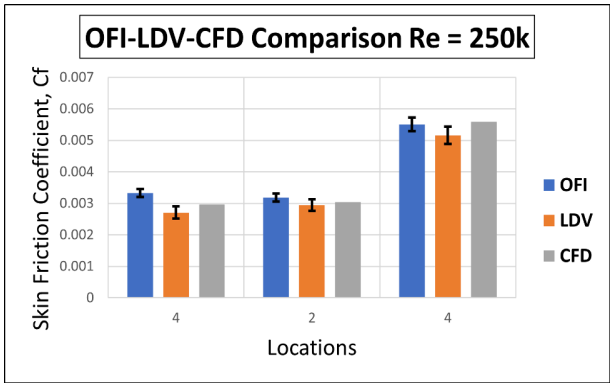

Fig. 23 Skin Friction Coefficient (C_f) comparisons between overlapping OFI, LDV and CFD.

VI. Conclusion

Skin friction measurements have been carried out as part of a benchmark study that aims to develop detailed experimental data for CFD validation. These measurements were taken on the BeVERLI hill model at various critical flow regions and at three Reynolds numbers based on the model's height. Oil Film Interferometry was used to obtain experimental data in terms of fringe images. Instrumentation and the experimental setups were explained in detail, along with a step-by-step data processing methodology. An uncertainty quantification procedure was implemented in this study with an emphasis on instrumentation and human errors. Experimental results were qualitatively and quantitatively discussed at various critical regions of the flow domain at three Reynolds numbers of 250,000, 325,000 and 650,000. Qualitative results from OFI were used as a primitive flow visualisation method to understand local flow directions, separation region, and the general wall shear stress trends on the hill. Quantitative results strengthened

our understanding of wall shear stresses through C_f values along the hill. This further helped in understanding flow symmetry and asymmetry in the hill's inflow and wake regions.

The skin friction results from OFI were then compared to that of Laser Doppler Velocimetry at three overlapping measurement locations and at two Reynolds numbers. The variations between the two data sets were discussed, along with their respective uncertainties. This comparison strengthened the confidence in the results from OFI with a considerable close agreement between the results of the two measurement techniques. Brief suggestions on how the two measurements complement each were also discussed. A CFD validation study was performed using the results from a RANS k-ω SST simulation and the difference of the prediction of flow physics by the CFD and experiments were observed and discussed through C_f. An excellent general agreement between OFI and CFD was noticed, except for a few inflow locations at lower Reynolds number and the wake regions at high Reynolds numbers. Finally, available LDV C_f data was compared with the OFI and CFD results, and a good agreement between the three data sets was observed.

VII. Acknowledgements

The researchers at Virginia Tech would like to thank NASA, in particular Dr. Michael Kegerise, Dr. Mujeeb Malik, and Dr. Christopher Rumsey, for their assistance under grant number 80NSSC18M0146. We are grateful for the contributions of Bill Oetjens, Dr. Vidya Vishwanathan, Daniel Binu, and Will Jordan to wind tunnel testing and OFI data processing. We would also like to thank the Virginia Tech Aerospace and Ocean Engineering Machine Shop, and particularly James Lambert, Cameron Hollandsworth, and John Burleson, for their support in designing and manufacturing test hardware and instrumentation.

References

[1] Hoerner, S. F., "Fluid-dynamic drag," *Hoerner fluid dynamics*, 1965.

[2] Kim, K.-S., and Settles, G. S., "Skin friction measurements by laser interferometry in swept shock/boundary-layer interactions," *AIAA Journal*, Vol. 28, No. 1, 1990, pp. 133–139.

[3] Kim, K.-S., Lee, Y., Alvi, F., Settles, G., and Horstman, C., "Skin-friction measurements and computational comparison of swept shock/boundary-layer interactions," *AIAA journal*, Vol. 29, No. 10, 1991, pp. 1643–1650.

[4] Brown, J. L., and Naughton, J. W., "The thin oil film equation," Tech. rep., 1999.

[5] Naughton, J. W., and Sheplak, M., "Modern developments in shear-stress measurement," *Progress in Aerospace Sciences*, Vol. 38, No. 6-7, 2002, pp. 515–570.

[6] Naughton, J. W., Viken, S., and Greenblatt, D., "Skin friction measurements on the NASA hump model," *AIAA journal*, Vol. 44, No. 6, 2006, pp. 1255–1265.

[7] Driver, D. M., "Application of oil-film interferometry skin-friction measurement to large wind tunnels," *Experiments in fluids*, Vol. 34, No. 6, 2003, pp. 717–725.

[8] Johansson, G., Naughton, J., Mehdi, F., and Shiri, F., "Skin friction measurements using oil film interferometry and laser Doppler anemometry," *4th AIAA Theoretical Fluid Mechanics Meeting*, 2005, p. 4673.

[9] Driver, D. M., and Drake, A., "Skin Friction Measurements Using Oil-Film Interferometry in NASA's 11-Foot Transonic Wind Tunnel," *AIAA journal*, Vol. 46, No. 10, 2008, pp. 2401–2407.

[10] Baldwin, A., Mears, L. J., Arora, N., Kumar, R., Alvi, F. S., and Naughton, J. W., "Skin friction measurements using oil film interferometry in a 3-d supersonic flowfield," *AIAA Journal*, Vol. 57, No. 4, 2019, pp. 1373–1382.

[11] Gargiulo, A., Beardsley, C., Vishwanathan, V., Fritsch, D. J., Duetsch-Patel, J. E., Szoke, M., Borgoltz, A., Devenport, W. J., Roy, C. J., and Lowe, K. T., "Examination of Flow Sensitivities in Turbulence Model Validation Experiments," *AIAA SciTech 2020 Forum*, 2020, p. 1583.

[12] Lowe, T., Borgoltz, A., Devenport, W. J., Fritsch, D. J., Gargiulo, A., Duetsch-Patel, J. E., Roy, C. J., Szoke, M., and Vishwanathan, V., "Status of the NASA/Virginia Tech benchmark experiments for CFD validation," *AIAA SciTech 2020 Forum*, 2020, p. 1584.

[13] Oberkampf, W. L., and Smith, B. L., "Assessment criteria for computational fluid dynamics model validation experiments," *Journal of Verification, Validation and Uncertainty Quantification*, Vol. 2, No. 3, 2017.

[14] Gargiulo, A., Ozoroski, T. A., Hallock, T., Haghiri, A., Sandberg, R. D., Visonneau, M., Deng, G., Guilmineau, E., Geneau, D., Jeans, T., et al., "Computations of the BeVERLI Hill three-dimensional separating flow model validation cases," *AIAA SCITECH 2022 Forum*, 2022, p. 1034.

[15] Duetsch-Patel, J. E., MacGregor, D., Jenssen, Y. L., Henry, P.-Y., Muthanna, C., Savio, L., Lavoie, P., Gargiulo, A., Sundarraj, V., Ozoroski, T. A., et al., "The BeVERLI Hill three-dimensional separating flow case: cross-facility comparisons of validation experiment results," *AIAA SCITECH 2022 Forum*, 2022, p. 0698.

[16] Byun, G., Simpson, R. L., and Long, C., "Study of vortical separation from three-dimensional symmetric bumps," *AIAA journal*, Vol. 42, No. 4, 2004, pp. 754–765.

[17] Byun, G., and Simpson, R. L., "Structure of three-dimensional separated flow on an axisymmetric bump," *AIAA journal*, Vol. 44, No. 5, 2006, pp. 999–1008.

[18] Simpson, R. L., and Long, C. H., "Study of vortical separation from an axisymmetric hill," *Second Symposium on Turbulence and Shear Flow Phenomena*, Begel House Inc., 2001, pp. 65–70.

[19] Bell, J., Heineck, J., Zilliac, G., Mehta, R., and Long, K., "Surface and flow field measurements on the faith hill model," *50th AIAA Aerospace Sciences Meeting including the New Horizons Forum and Aerospace Exposition*, 2012, p. 704.

[20] Gargiulo, A., Duetsch-Patel, J. E., Ozoroski, T. A., Beardsley, C., Vishwanathan, V., Fritsch, D., Borgoltz, A., Devenport, W. J., Roy, C. J., and Lowe, K. T., "Flow Field Features of the BEVERLI Hill Model," *AIAA Scitech 2021 Forum*, 2021, p. 1741.

[21] Ozoroski, T. A., Gargiulo, A., Duetsch-Patel, J. E., Sundarraj, V., Roy, C. J., Devenport, W. J., Lowe, T., and Borgoltz, A., "CFD Analysis of the BeVERLI Hill Turbulence Model Validation Experiments," *AIAA SCITECH 2022 Forum*, 2022, p. 0050.

[22] Naughton, J. W., and Liu, T., "Photogrammetry in oil-film interferometry," *AIAA journal*, Vol. 45, No. 7, 2007, pp. 1620–1629.

[23] Duetsch-Patel, J. E., Vishwanathan, V., Minionis, J. B., Totten, E., Gargiulo, A., Fritsch, D. J., Szoke, M., Borgoltz, A., Roy, C. J., Lowe, K. T., et al., "Aerodynamic Design and Assessment of Modular Test Section Walls for CFD Validation in Hybrid Anechoic Wind Tunnels," *AIAA SciTech 2020 Forum*, 2020, p. 2214.

[24] Vishwanathan, V., Szoke, M., Duetsch-Patel, J. E., Gargiulo, A., Fritsch, D. J., Borgoltz, A., Roy, C. J., Lowe, K. T., and Devenport, W. J., "Aerodynamic design and validation of a contraction profile for flow field improvement and uncertainty quantification in a subsonic wind tunnel," *AIAA SciTech 2020 Forum*, 2020, p. 2211.

[25] Tanner, L., and Blows, L., "A study of the motion of oil films on surfaces in air flow, with application to the measurement of skin friction," *Journal of Physics E: Scientific Instruments*, Vol. 9, No. 3, 1976, p. 194.

[26] Naughton, J., Robinson, J., and Durgesh, V., "Oil-film interferometry measurement of skin friction-analysis summary and description of matlab program," *20th International Congress on Instrumentation in Aerospace Simulation Facilities, 2003. ICIASF'03.*, IEEE, 2003, pp. 169–178.

[27] Garrison, T., and Ackman, M., "Development of a global interferometer skin-friction meter," *AIAA journal*, Vol. 36, No. 1, 1998, pp. 62–68.

[28] "Philips Sodium Bulb - Product Description," `https://www.assets.lighting.philips.com/is/content/PhilipsLighting/comf1458-pss-en_ca`, N/A.

[29] "Sony Alpha 6500 - Camera Specifications," `https://www.sony.com/ng/electronics/interchangeable-lens-cameras/ilce-6500-body-kitl`, 2016.

[30] "Clearco Product Description," `http://www.clearcoproducts.com/pure-silicone-standard-viscosity.html`, N/A.

[31] Liu, T., Cattafesta III, L., Radeztsky, R., and Burner, A., "Photogrammetry applied to wind-tunnel testing," *AIAA Journal*, Vol. 38, No. 6, 2000, pp. 964–971.

[32] "Matlab Single Camera Calibrator Application," `https://www.mathworks.com/help/vision/ug/using-the-single-camera-calibrator-app.html`, N/A.

[33] Gluzman, I., Gray, P., Mejia, K., Corke, T. C., and Thomas, F. O., "A simplified photogrammetry procedure in oil-film interferometry for accurate skin-friction measurement over arbitrary geometries," *Experiments in Fluids*, Vol. 63, No. 7, 2022, pp. 1–14.

[34] Duetsch-Patel, J., Gargiulo, A., Borgoltz, A., Devenport, W., and Lowe, K., "Structural Aspects of the Attached Turbulent Boundary Layer Flow Over a Hill," *Experiments in Fluids*, Under Revision.

[35] Gargiulo, A., Duetsch-Patel, J., Borgoltz, A., Devenport, W., Roy, C., and Lowe, K., "Strategies for Computational Fluid Dynamics Validation Experiments," *TBA*, TBA.

VIII. Appendix

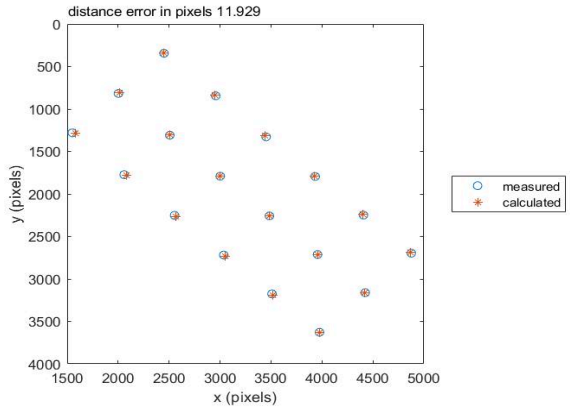

Fig. 24 Results from the extrinsic camera calibration step showing measured and calculated points as well as distance error in pixels.

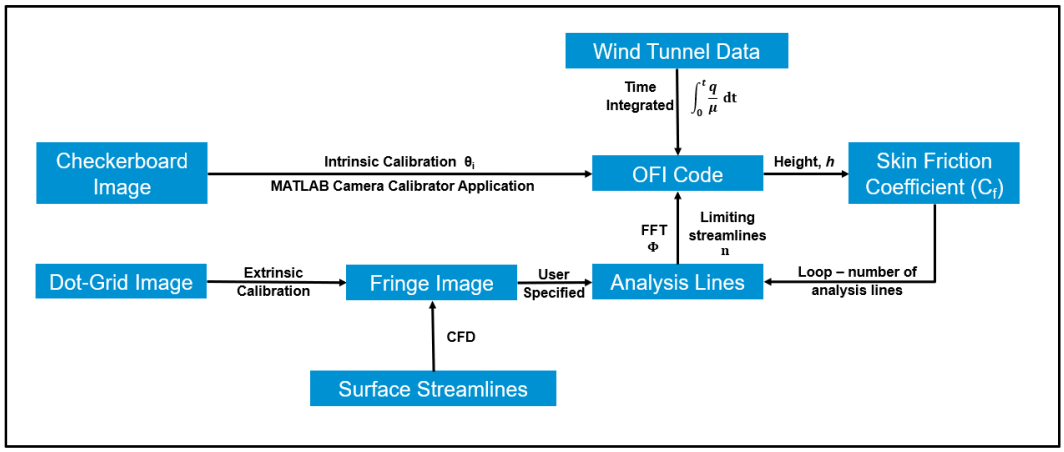

Fig. 25 OFI data processing steps in the form of a flowchart.